NMR Imaging of Catalytic Hydrogenation in Microreactors with the Use of para-Hydrogen

Louis-S. Bouchard, *et al.*

Science **319**, 442 (2008);
DOI: 10.1126/science.1151787

$^3O_2$ with bulk Al (*30*) and with the Al_{13}^- cluster. Because the interpretation of the low bulk reactivity remains unsettled, the results presented here may prove useful in unraveling the controversy surrounding the interpretation of solid-state aluminum reactivity. Furthermore, spin states play an important role in long-known oxidation processes (e.g., O_2/NO/NO_2; O_2/SO_2/SO_3), and also in the oxidation of carbon compounds: The first detailed experimental and theoretical data for $^1O_2$ reactions with 2 + 4 and 2 + 2 cycloadditions were presented only a decade ago (*28*). Thus, the present results may initiate further FT-ICR investigations of $^1O_2$ and $^3O_2$ reactions in many other chemical oxidation processes that affect our daily lives, e.g., in biology (respiration), engineering (corrosion), and energetics (combustion).

References and Notes

1. M. Brack, *Rev. Mod. Phys.* **65**, 677 (1993).
2. W. A. de Heer, *Rev. Mod. Phys.* **65**, 611 (1993).
3. T. P. Martin, *Phys. Rep.* **273**, 199 (1996).
4. R. Ahlrichs, S. D. Elliott, *Phys. Chem. Chem. Phys.* **1**, 13 (1999).
5. X. Li, H. Wu, X.-B. Wang, L.-S. Wang, *Phys. Rev. Lett.* **81**, 1909 (1998).
6. D. E. Bergeron, A. W. J. Castleman, T. Morisato, S. N. Khanna, *Science* **304**, 84 (2004).
7. M. F. Jarrold, J. E. Bower, *Chem. Phys. Lett.* **144**, 311 (1988).
8. R. E. Leuchtner, A. C. Harms, A. W. Castleman Jr., *J. Chem. Phys.* **94**, 1093 (1991).
9. R. L. Hettich, *J. Am. Chem. Soc.* **111**, 8582 (1989).
10. C. Ashman, S. N. Khanna, M. R. Pederson, *Chem. Phys. Lett.* **324**, 137 (2000).
11. We use the abbreviations Al_{even} and Al_{odd} to denote Al_n^- clusters with an even or odd number of Al atoms. The spin multiplicities of molecular entities are denoted by superscription, e.g., triplet oxygen by $^3O_2$.
12. A. C. Reber, S. N. Khanna, P. J. Roach, W. H. Woodward, A. W. Castleman Jr., *J. Am. Chem. Soc.* **129**, 16098 (2007).
13. R. Burgert, H. Schnöckel, M. Olzmann, K. H. Bowen Jr., *Angew. Chem. Int. Ed.* **45**, 1476 (2006).
14. R. Burgert, S. T. Stokes, K. H. Bowen, H. Schnöckel, *J. Am. Chem. Soc.* **128**, 7904 (2006).
15. M. W. Chase Jr., in *NIST-JANAF Thermochemical Tables, J. Phys. Chem. Ref. Data, Monograph 9*. (1998), pp. 1–1951.
16. R. E. Leuchtner, A. C. Harms, A. W. Castleman Jr., *J. Chem. Phys.* **91**, 2753 (1989).
17. G. H. Peslherbe, W. L. Hase, *J. Phys. Chem. A* **104**, 10556 (2000).
18. Although neutral species cannot be directly observed in our experiment, Al_2O, as the likely neutral by-product of the oxidation of Al clusters, was indirectly inferred from the following: (i) By performing the experiments under ultralow-pressure conditions, one can ensure that only few collisions of clusters with O_2 occur (~1 per second), thereby excluding the possibility of involvement of more than one O_2 molecule per reaction event. Consequently, observing that oxidation of Al_n^- clusters yields $Al_{(n-4)}^-$ implies concomitant formation of a neutral fragment, Al_4O_2, or several fragments stoichiometrically equivalent to Al_4O_2. (ii) According to the phase space theory, the validity of which was confirmed for Al clusters (*17*), the formation of Al_4O_2 (instead of two Al_2O) is unlikely, because the average lifetime of an $Al_{13}O_2^-$ or $Al_{14}O_2^-$ adduct with respect to this reaction channel is estimated to be some years (see calculations in SOM Text, section 2). (iii) The formation of Al atoms during degradation of the $Al_{13}O_2^-$ clusters toward Al_9^- can be excluded by thermodynamical reasons (SOM Text, section 3).
19. E. G. Mednikov, M. C. Jewell, L. F. Dahl, *J. Am. Chem. Soc.* **129**, 11619 (2007).
20. H. Schwarz, *Int. J. Mass Spectrom.* **237**, 75 (2004).
21. X. Li *et al.*, *Science* **315**, 356 (2007).
22. H. Okabe, in *Photochemistry of Small Molecules* (Wiley, New York, 1978), pp. 431–432.
23. R. Ahlrichs, C. Ehrhardt, M. Lakenbrink, S. Schunck, H. Schnöckel, *J. Am. Chem. Soc.* **108**, 3596 (1986).
24. Because there is a large excess of O_3 compared to the Al cluster anions, too few $^1O_2$ molecules are formed as coproducts to induce undesired reactions.
25. M. J. Frisch *et al.*, Gaussian 03, Revision C.02; Gaussian, Inc., Wallingford, CT (2004).
26. All the CCSD(T) calculations were done with NWChem 5.1 using the Computers at Molecular Science Computing Facility (MCSF) in Environmental Molecular Science Laboratory (EMSL), a national scientific user facility sponsored by the U.S. Department of Energy (DOE), Office of Biological and Environmental Research (OBER), and located at Pacific Northwest National Laboratory.
27. W. Adam, *Chem. Unserer Zeit* **15**, 190 (1981).
28. A. Greer, *Acc. Chem. Res.* **39**, 797 (2006).
29. There is a lack of reliable methods to calculate the height of this barrier. However, for similar reactions in organic chemistry, this barrier is indicated to be 0.8 eV (*27*).
30. J. Behler, B. Delley, S. Lorenz, K. Reuter, M. Scheffler, *Phys. Rev. Lett.* **94**, 036104/1 (2005).

31. H.S. acknowledges M. Olzmann for helpful discussions. H.S. and G.F.G. thank the Deutsche Forschungsgemeinschaft (DFG) and the DFG–Center for Functional Nanostructures (H.S.) for their support of this work. K.H.B. thanks the Air Force Office of Scientific Research for its support. P.J. thanks the U.S. DOE for its support.

Supporting Online Material

www.sciencemag.org/cgi/content/full/319/5862/438/DC1
SOM Text
Figs. S1 to S3
Table S1
References

1 August 2007; accepted 14 December 2007
10.1126/science.1148643

NMR Imaging of Catalytic Hydrogenation in Microreactors with the Use of para-Hydrogen

Louis-S. Bouchard,[1]* Scott R. Burt,[1] M. Sabieh Anwar,[2] Kirill V. Kovtunov,[3] Igor V. Koptyug,[3] Alexander Pines[1]*

Catalysis is vital to industrial chemistry, and the optimization of catalytic reactors attracts considerable resources. It has proven challenging to correlate the active regions in heterogeneous catalyst beds with morphology and to monitor multistep reactions within the bed. We demonstrate techniques, using magnetic resonance imaging and para-hydrogen (p-H_2) polarization, that allow direct visualization of gas-phase flow and the density of active catalyst in a packed-bed microreactor, as well as control over the dynamics of the polarized state in space and time to facilitate the study of subsequent reactions. These procedures are suitable for characterizing reactors and reactions in microfluidic devices where low sensitivity of conventional magnetic resonance would otherwise be the limiting factor.

Catalysis is a fundamental component to many industrial processes and, consequently, the optimization of catalytic reactions and reactors attracts considerable technological effort and financial commitments. An important aspect of this optimization is to correlate the spatial distribution of the reactive conversion inside the reactor with the morphology and packing of the catalyst. Here, we describe a spectroscopic method for this purpose based on magnetic resonance imaging (MRI) (*1*) that uses hyperpolarized spins derived from p-H_2 (*2*, *3*). Specifically, we achieve high-resolution, spatially resolved profiles of heterogeneous hydrogenation reactions taking place at a solid-gas interface inside a microreactor. We demonstrate strongly enhanced nuclear magnetic resonance (NMR) signal intensities in the gas phase as well as precise control over the spatiotemporal dynamics of the polarization. The enhanced sensitivity is particularly important for tracking gases and products in small volumes [e.g., in microfluidic devices (*4*, *5*) or the limited void space of a tightly packed catalyst bed]. Moreover, the controlled delivery of p-H_2–induced nuclear spin polarization acts as a spin label that can transport polarization to remote regions in the reactor. This work has implications for studying kinetics and mechanisms of multistep heterogeneously catalyzed reactions and fluid-flow transport, as well as mass and heat transfer. Such characterization should facilitate improved reactor and catalyst design.

Methods to optimize microreactors would be welcome in the context of microfluidic (lab-on-a-chip) technology. In recent years, the compelling advantages of microfluidic technology (*4*, *5*) in biopharmaceutical applications, chemical analysis (*6*), organic synthesis (*7*, *8*), and industrial catalysis have been recognized and demonstrated

[1]Materials Sciences Division, Lawrence Berkeley National Laboratory and Department of Chemistry, University of California, Berkeley, CA 94720, USA. [2]School of Science and Engineering, Lahore University of Management & Sciences, Opposite Sector U, D.H.A., Lahore 54792, Pakistan. [3]International Tomography Center, 3A Institutskaya Street, Novosibirsk 630090, Russia.

*To whom correspondence should be addressed. E-mail: louis.bouchard@gmail.com (L.-S.B.); pines@berkeley.edu (A.P.)

(*9*, *10*). These include smaller volumes and substantial economic savings, precise control of reactant delivery, improved fluid transport and heat dispersion, control of reaction rates, enhanced safety of highly exothermic or explosive processes, and the possibility of faster reactions, improved yield, and chemoselectivity. Recent developments in microfluidic technology also provide powerful means for performing complex reactions, such as multistep transformations (*9*) or multiphase reactions (*10*). Furthermore, the use of catalysts immobilized on solid supports in flow-mode microreactors has recently been shown to result in highly efficient reactions (*10*, *11*).

One important characterization for the optimization of catalyst bed reactors is the flow map. Knowledge of the velocity distribution of the reaction product enables study of transport phenomena within a microreactor (*12*–*14*) and optimization of the catalyst packing and reactor geometry. High flow uniformity in a catalytic converter is crucial for avoiding non-uniform deactivation of the catalyst caused by both chemical and thermal aging. With the increasing sophistication of mathematical modeling, such systems are routinely characterized by computational fluid dynamics. However, the relevance of such models is in doubt until they are validated against real measurements (*15*). This is particularly difficult in packed-bed microreactors where the methods available are limited to tracers and bulk (average) properties of temperature, conversion, and velocity. Despite the need for validation, the spatiotemporal distribution of reactants and products in heterogeneous systems has been seldom visited by chemical engineering researchers in recent years, owing to the substantial difficulties with performing quantitative measurements in situ (*15*).

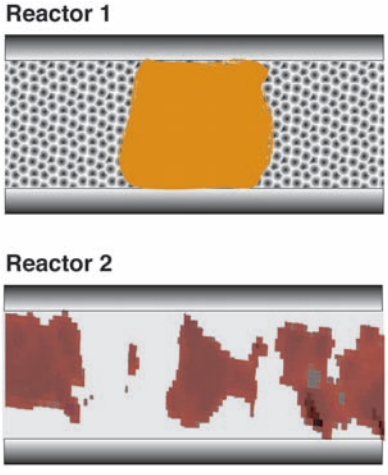

Fig. 1. Schematic of the microreactors. The two model catalytic reactors consist of catalyst layers sandwiched between layers of glass beads for stability. Reactor 1 contains a thin layer of silica gel–supported Wilkinson's catalyst (orange). Reactor 2 contains powdered Wilkinson's catalyst (red) arrayed in variously sized clumps to demonstrate a more heterogeneous scenario.

Various techniques have been used to study the motion of fluids in catalytic processes. For example, capacitance (*16*), single-photon emission–computed tomography (*17*), and positron emission tomography (*18*) are used to monitor gas-liquid distributions in multiphase reactors. But these methods measure average flow properties and have limited spatial resolution. The use of MRI to characterize microreactors is advantageous because the technique is noninvasive, can probe optically opaque media, and is appealing for catalysis because of the variety of molecular parameters that can be mapped with considerable chemical and spatial selectivity (*19*). Specifically, flow maps and local density profiles can be generated, molecular mobility can be tracked, and chemical reaction mechanisms can be probed with spin-labeled nuclei (*20*). Previous applications of MRI to heterogeneous catalysis included studies of hydrogenation processes without p-H_2 (*21*, *22*), catalyst morphologies and synthesis

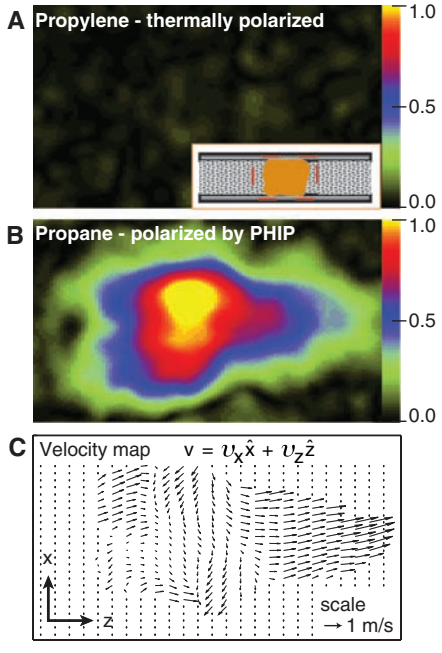

Fig. 2. Density of active catalyst and flow map imaging. MRI images [field of view (FOV) (*x* to *z*): 2.3 mm by 7.0 mm; pixel size: 20 μm by 60 μm] of a tightly packed catalyst bed (catalyst layer thickness is ~5 mm) are shown. (**A**) Thermally polarized propylene. The approximate position of the imaging FOV is indicated by the dashed red lines in the inset. (**B**) p-H_2–polarized propane. The signal-to-noise ratio (SNR) of this image is a factor of 300 larger than that of the thermally polarized propylene image. (**C**) Flow map in the *xz* plane with the use of polarized propane. The orientation of the arrows represents direction of the velocity, and their length represents its magnitude. The SNR of thermally polarized propylene was insufficient to generate a velocity map. The resolution of the flow map is intentionally decreased by retaining only 1 of every 16 arrows to avoid excessive overlap of the arrows.

techniques (*23*, *24*), and fluid flow through the catalyst bed (*25*), as well as monitoring of esterification reactions (*12*, *13*) in situ. All of these applications were based on the NMR signal detection of the liquid phase and thus offer a sensitivity that is three orders of magnitude larger as compared with gases, resulting from the difference in density. The sensitivity enhancement offered by p-H_2–induced polarization (PHIP) is essential for the application of MRI to heterogeneous chemical reactions in the gas phase.

p-H_2 (*2*, *3*, *26*) is characterized by a singlet nuclear spin wave function and is relatively easy to prepare in quantum-state ensembles of very high purity. The total nuclear spin angular momentum of this state is zero, resulting in no observable NMR signal. However, if the protons participate in pairwise hydrogenation in which they become magnetically inequivalent, strong observable magnetization can be produced (*2*, *3*, *26*) with a signal enhancement factor typically on the order of 10^4. For instance, if p-H_2 is used in the hydrogenation of propylene into propane (*27*, *28*), the p-H_2–derived protons will be in the singlet state immediately after the transformation of the substrate molecule into the product molecule. Typically, the molecular additions occur at randomly distributed times, and the result is an incoherent but highly polarized nuclear spin state. Application of suitable radio-frequency (rf) pulses results in a hyperpolarized NMR signal (*29*). However, if an isotropic mixing sequence is applied during the course of the reaction, not only is a coherent singlet state preserved, but the lifetime of this state is also increased (*30*). As we demonstrate below, this effect allows one to create a relatively long-lived, coherent packet of polarized product molecules, which augments the versatility of this technique beyond hydrogenation reactions.

To demonstrate the effectiveness of heterogeneously catalyzed PHIP in microreactors, we use two model catalytic reactors (*29*) (Fig. 1). In both cases, propylene and p-H_2 gases are flowed through the catalyst bed and react to form propane. The first reactor (reactor 1) contains a tightly packed bed of the silica gel–immobilized Wilkinson's catalyst located between two layers of glass beads. This reactor is used to produce a highly polarized product (propane) and illustrates the ability to resolve flow maps, active regions in the catalyst bed, and controlled transport of polarization out of the catalyst bed. The second reactor (reactor 2) comprises powdered Wilkinson's catalyst loosely packed with some small (~2-mm) air gaps. This second reactor further demonstrates the control of a polarized outstream and applications to a more heterogeneous packing.

The PHIP signal in these experiments is larger than the corresponding thermal signal by a factor of 300 (*29*). This enhancement is crucial in light of the coil-sample arrangement. The ratio of the rf coil volume occupied by the microchannel to the rf coil volume is less than 0.01: a situation that is unfavorable in terms of detection

sensitivity. Furthermore, the presence of catalyst powder occludes the space inside the microchannel. This sensitivity loss, combined with the low density of the gas, leads to a million-fold loss in sensitivity relative to standard liquid-state NMR. Our experimental results show that PHIP can, to a large extent, circumvent the problem of low sensitivities in gas-phase microreactors.

An image of the first reactor is shown in Fig. 2. The spatial distribution of reactant (propylene) is barely resolved (Fig. 2A), whereas the polarized product (propane) shows a strongly enhanced signal (Fig. 2B). We also compare a spectrum from the reactor (fig. S2A) and localized spectra from upstream of (fig. S2B) and in (fig. S2C) the catalyst bed. The use of a hyperpolarized substance was also necessary for producing the high-resolution gas-phase flow map shown in Fig. 2C (*29*). This example reveals heterogeneous flow patterns in the catalyst bed, which are consistent with a non-uniform packing of the catalyst (*29*), that are not apparent in Fig. 2B. Flow imaging at the same resolution and sensitivity would not be possible with the exceedingly weak thermal signals.

As illustrated in Fig. 3A, the residence time inside the tightly packed region leads to nearly complete magnetic relaxation, and no polarized product is observed beyond the catalyst bed. Although this outcome is ideal for imaging the active regions of the catalyst bed, the polarized spins cannot be used for subsequent reactions. Isotropic mixing sequences have been shown to prolong the lifetime of the nuclear spin-singlet state (*30*). Thus, the use of an isotropic mixing sequence (*31*) applied for a sufficiently long duration T_m allows the polarized product to escape the catalyst bed (the optimal T_m will depend on the average flow velocity v). This period is followed by a delay T_d, allowing the singlet state to travel a distance $x = v \times T_d$, during which the singlet state evolves into a state observable by NMR. By varying T_d, we control the distance traveled before the polarization is released. Figure 3, B and C, demonstrates the delivery of polarized product beyond the catalyst bed for two values of T_d.

Imaging of the second reactor (Fig. 4A) further demonstrates the usefulness of controlling the polarized outstream. In contrast with the packing in reactor 1, the looser packing in reactor 2 results in a polarized product that can be seen escaping the first catalyst layer and flowing to the second layer in the absence of singlet state preservation (T_m = 0 ms, T_d = 0 ms). Although this situation is desirable when the polarized product is to be used in subsequent reactions, it is problematic as a means for imaging the catalyst layer because of poor contrast and blurring from the uncontrolled flow of polarized product. This drawback can be remedied by controlling the singlet state as follows. For short values of T_d (1 ms), no polarized product can be seen between the catalyst layers, because the singlet state has not yet evolved into an observable state. At longer time intervals (T_d = 100 ms), the polarized product has traversed longer distances and evolved into an observable polarized product. A photograph of the reactor (Fig. 4B) provides a comparison of the distribution of catalyst in the reactor with the structural morphology observed in the MRI images.

Regardless of the packing, singlet state preservation provides a distinctive method for controlled delivery of polarization. Combined with knowledge of the local flow velocity, the timed release of polarization can be performed in remote parts of a microreactor. Thus, in multistep reactions, the polarized product can be used as a spin label to elucidate subsequent stages of a reaction (*20*).

These experiments can be extended by means of a variety of polarization transfer and spin manipulation methods to move the enhanced signal to other NMR-active nuclei on the substrate molecule or onto the catalyst itself (*14*, *20*). Transfer of polarization to heteronuclei yields a larger range of chemical shifts as compared with that of protons (*14*). The highly polarized spin product also makes it possible to image flows (*32*) and reactions (*33*) in precisely engineered microchannels noninvasively, opening the way for a variety of microfluidic applications.

There are still many challenges to address before these results can be extended to a wider range of hydrogenation reactions and conditions of industrial catalytic processes. In particular, it remains to be seen to what extent the polarization lifetimes and the NMR linewidths of the reaction products are affected by the presence of metal catalyst surfaces, microscopic gradients of magnetic susceptibility, high temperatures, paramagnetic catalysts and impurities, liquid films, and other complications that can be expected under conditions encountered in practice. To this end, recent results (*34*) that demonstrate PHIP in heterogeneous hydrogenations catalyzed by supported metal catalysts (Pt/Al_2O_3 and Pd/Al_2O_3) are encouraging.

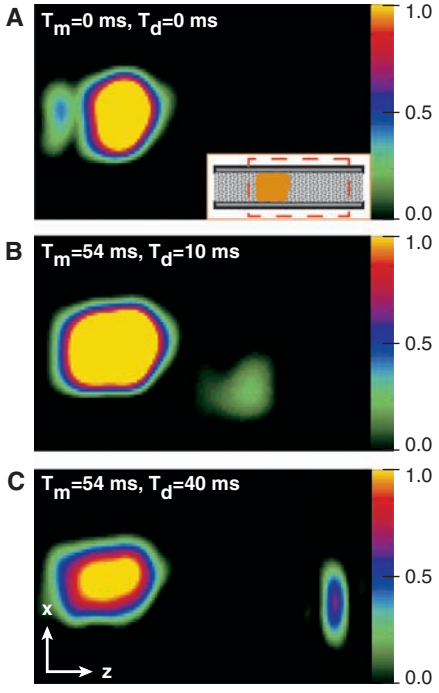

Fig. 3. Controlled transport of polarized product. MRI images [FOV (*x* to *z*): 8.5 mm by 23 mm; pixel size: 0.5 mm by 1 mm] for different travel times after an isotropic mixing sequence are shown. (**A**) No isotropic mixing: The polarized product is observed only in the catalyst layer. The approximate position of the imaging FOV is indicated by the dashed red lines in the inset. (**B**) Ten milliseconds after isotropic mixing, the polarized product travels 5 mm. (**C**) Forty milliseconds after isotropic mixing, the product has traveled 10 mm.

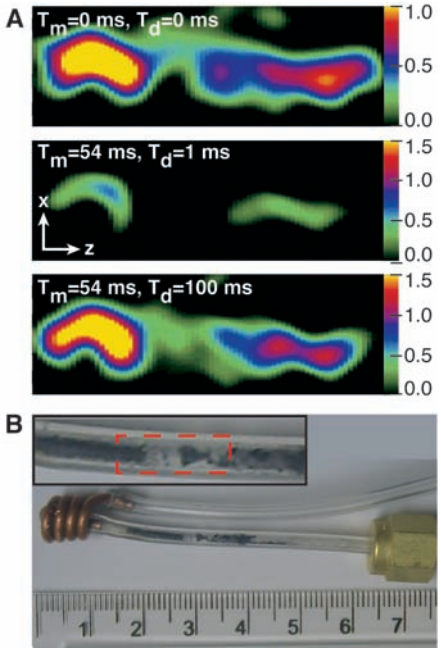

Fig. 4. Imaging heterogeneous distributions of catalyst. (**A**) MRI images [FOV (*x* to *z*): 2 mm by 15 mm; pixel size: 0.4 mm by 0.9 mm] of the heterogeneous packing, acquired without isotropic mixing (T_m = 0 ms, T_d = 0 ms) and for two different travel time intervals (T_d = 1 and 100 ms) after 54 ms of isotropic mixing. (**B**) Catalytic reactor containing a heterogeneous packing of Wilkinson's catalyst powder mixed with glass beads. An enlarged view of the catalyst packing is shown in the inset. The dashed red lines indicate the approximate location of the FOV for the images in (A).

References and Notes

1. P. C. Lauterbur, *Nature* **242**, 190 (1973).
2. J. Natterer, J. Bargon, *Prog. Nucl. Magn. Reson. Spectrosc.* **31**, 293 (1997).
3. C. R. Bowers, D. P. Weitekamp, *Phys. Rev. Lett.* **57**, 2645 (1986).
4. G. M. Whitesides, *Nature* **442**, 368 (2006).
5. H. Craighead, *Nature* **442**, 387 (2006).
6. D. Belder, *Anal. Bioanal. Chem.* **385**, 416 (2006).
7. P. Watts, S. J. Haswell, *Chem. Eng. Technol.* **28**, 290 (2005).
8. S. J. Haswell *et al.*, *Chem. Commun.* **2001**, 391 (2001).
9. B. Ahmed-Omer, J. C. Brandt, T. Wirth, *Org. Biomol. Chem.* **5**, 733 (2007).
10. J. Kobayashi *et al.*, *Science* **304**, 1305 (2004).
11. A. R. Bogdan, B. P. Mason, K. T. Sylvester, D. T. McQuade, *Angew. Chem. Int. Ed.* **46**, 1698 (2007).

12. E. H. L. Yuen, A. J. Sederman, L. F. Gladden, *Appl. Catal. Gen.* **232**, 29 (2002).
13. M. Küppers, C. Heine, S. Han, S. Stapf, B. Blümich, *Appl. Magn. Reson.* **22**, 235 (2002).
14. M. Haake, J. Natterer, J. Bargon, *J. Am. Chem. Soc.* **118**, 8688 (1996).
15. D. Tayebi, H. F. Svendsen, H. A. Jakobsen, A. Grislingås, *Chem. Eng. Comm.* **186**, 56 (2001).
16. D. Mewes, T. Loser, M. Millies, *Chem. Eng. Sci.* **54**, 4729 (1999).
17. T. Bauer, S. Roy, R. Lange, M. Al-Dahhan, *Chem. Eng. Sci.* **60**, 3101 (2005).
18. D. J. Parker, P. A. McNeil, *Meas. Sci. Technol.* **7**, 287 (1996).
19. P. T. Callaghan, *Principles of Nuclear Magnetic Resonance Microscopy* (Oxford Univ. Press, New York, 1993).
20. M. S. Anwar *et al.*, *Anal. Chem.* **79**, 2806 (2007).
21. I. V. Koptyug, A. A. Lysova, R. Z. Sagdeev, V. N. Parmon, *Catal. Today* **126**, 37 (2007).
22. A. J. Sederman, M. D. Mantle, C. P. Dunckley, Z. Huang, L. F. Gladden, *Catal. Lett.* **103**, 1 (2005).
23. I. V. Koptyug, D. R. Sagdeev, E. Gerkema, H. Van As, H. R. Z. Sagdeev, *J. Magn. Reson.* **175**, 21 (2005).
24. A. A. Lysova *et al.*, *J. Am. Chem. Soc.* **127**, 11916 (2005).
25. A. A. Lysova *et al.*, *Chem. Eng. J.* **130**, 101 (2007).
26. C. R. Bowers, in *Encyclopedia of Nuclear Magnetic Resonance*, D. M. Grant, R. K. Harris, Eds. (Wiley, Chichester, UK, vol. 9, 2002), pp. 750–770.
27. I. V. Koptyug *et al.*, *J. Am. Chem. Soc.* **129**, 5580 (2007).
28. L.-S. Bouchard *et al.*, *Angew. Chem. Int. Ed.* **46**, 4064 (2007).
29. Materials and methods are available as supporting material on *Science* Online.
30. M. Carravetta, O. G. Johannessen, M. H. Levitt, *Phys. Rev. Lett.* **92**, 153003 (2004).
31. A. J. Shaka, C. J. Lee, A. Pines, *J. Magn. Reson.* **77**, 274 (1988).
32. S. Ahola *et al.*, *Lab Chip* **6**, 90 (2006).
33. L. Ciobanu, D. A. Jayawickrama, X. Zhang, A. G. Webb, J. V. Sweedler, *Angew. Chem. Int. Ed.* **42**, 4669 (2003).
34. K. V. Kovtunov, I. E. Beck, V. I. Bukhtiyarov, I. V. Koptyug, *Angew. Chem. Int. Ed.*, in press (10.1002/anie.200704881).

35. This work was supported by the Director, Office of Science, Office of Basic Energy Sciences, Materials Sciences and Engineering Division, of the U.S. Department of Energy (DOE) under contract no. DE-AC03-76SF00098 and was partially supported by grants from the Russian Foundation for Basic Research (05-03-32472 and 07-03-12147), Siberian Branch of the Russian Academy of Sciences (integration grant no. 11), and Russian Academy of Sciences (5.1.1 and 5.2.3). S.R.B. thanks the U.S. Department of Homeland Security for support through a graduate fellowship, administered by the Oak Ridge Institute for Science and Education under the DOE contract number DE-AC05-06OR23100. I.V.K. thanks the Russian Science Support Foundation for financial support. The authors acknowledge R. Bergman, D. Wemmer, D. Budker, and J. Reimer for useful discussions and critical reading of the manuscript.

Supporting Online Material

www.sciencemag.org/cgi/content/full/319/5862/442/DC1
Materials and Methods
Figs. S1 and S2
References

16 October 2007; accepted 10 December 2007
10.1126/science.1151787

GaN Photonic-Crystal Surface-Emitting Laser at Blue-Violet Wavelengths

Hideki Matsubara,[1,2] Susumu Yoshimoto,[1] Hirohisa Saito,[1] Yue Jianglin,[1,2] Yoshinori Tanaka,[1,2] Susumu Noda[1,2,3]*

Shorter-wavelength surface-emitting laser sources are important for a variety of fields, including photonics, information processing, and biology. We report on the creation of a current-driven blue-violet photonic-crystal surface-emitting laser. We have developed a fabrication method, named "air holes retained over growth," in order to construct a two-dimensional gallium nitride (GaN)/air photonic-crystal structure. The resulting periodic structure has a photonic-crystal band-edge effect sufficient for the successful operation of a current-injection surface-emitting laser. This represents an important step in the development of laser sources that could be focused to a size much less than the wavelength and be integrated two-dimensionally at such short wavelengths.

The lasing principle of photonic-crystal surface-emitting lasers (PC-SELs) (*1*–*5*) is based on the band-edge effect in a two-dimensional (2D) PC, where the group velocity of light becomes zero and a 2D cavity mode is formed. The output power is coupled to the vertical direction by the PC itself, which gives rise to the surface-emitting function. PC-SELs have the following features: first, perfect, single longitudinal and lateral mode oscillation can be achieved even when the lasing area becomes very large (for example, devices >300 μm in diameter) (*1*, *3*, *5*); second, the polarization mode (*3*) and the beam pattern (*5*) can be controlled by appropriate design of the unit cell and/or lattice phase in the 2D PC. However, the shortest lasing wavelength achieved so far is 980 nm. A lasing wavelength in the blue-to-ultraviolet region would open the door to a much broader range of applications such as super–high-resolution laser sources, which can be focused to spot sizes smaller than blue-violet wavelengths by the use of doughnut beams (*5*, *6*), and optical tweezers for ultrafine manipulation.

One issue in the creation of a gallium nitride (GaN)–based PC-SEL has been whether a 2D PC structure could be constructed with a sufficient band-edge effect. To do so requires the fabrication of a high-quality 2D GaN/air periodic struc-

[1]Department of Electronic Science and Engineering, Kyoto University, Kyoto 615-8510, Japan. [2]Japan Science and Technology Agency, Kyoto 615-8510, Japan. [3]Photonics and Electronics Science and Engineering Center, Kyoto University, Kyoto 615-8510, Japan.

*To whom correspondence should be addressed. E-mail: snoda@kuee.kyoto-u.ac.jp

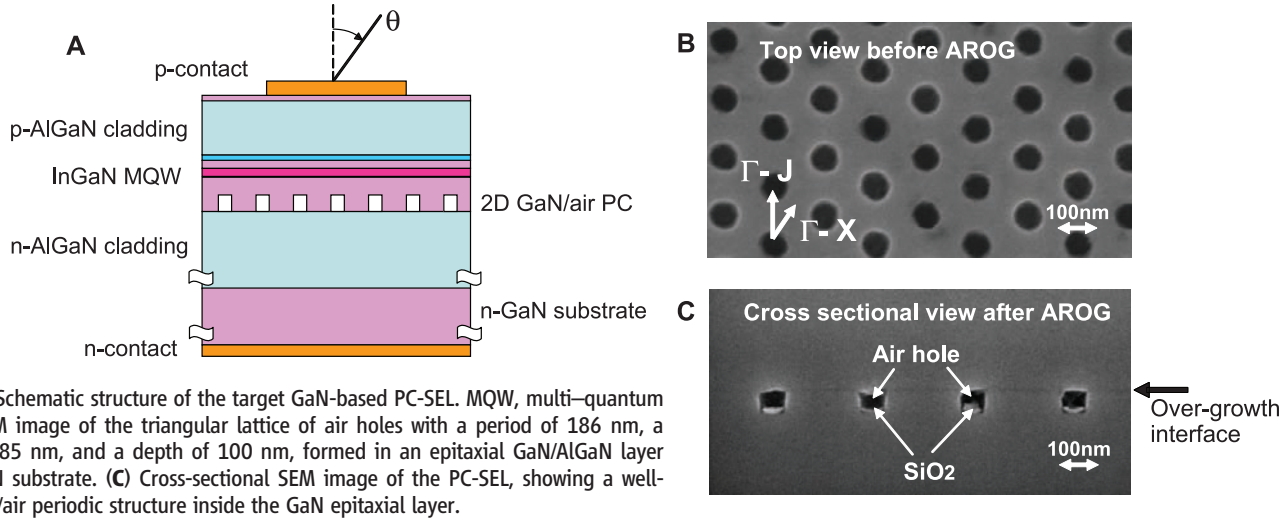

Fig. 1. (**A**) Schematic structure of the target GaN-based PC-SEL. MQW, multi–quantum well. (**B**) SEM image of the triangular lattice of air holes with a period of 186 nm, a diameter of 85 nm, and a depth of 100 nm, formed in an epitaxial GaN/AlGaN layer above a GaN substrate. (**C**) Cross-sectional SEM image of the PC-SEL, showing a well-defined GaN/air periodic structure inside the GaN epitaxial layer.